Chapter 1 Introduction and Literature Review

1.1 Introduction

Recent years have witnessed a vast surge of interest in the hexaferrites because of the discovery of multiferroicity and quantum phenomena in these compounds [1–10]. Amongst the various M-, Y-, U-, X-, W-, and Z-type hexaferrites, M-type hexaferrites are extensively used as permanent magnetic material in motors, generators, transformers, actuators, information storage, communications, civil transport, defence armaments and aerospace structures with market share worth $4 billion dollars [11–13]. Along with the wide variety of applications, M-type hexaferrites also exhibit several exotic phenomenons at very low temperatures such as quantum paraelectricity (QPE) [7,14,15], frustrated anti-ferroelectric state (AFE) [16], quantum electric dipole liquid state (QEDL) [7], spin-glass (SG) [17–26], spin liquid [18,24,27], quantum tunneling of magnetization [28], and multiferroicity [29–33]. These phenomena are of great interest in the field of materials science and solid-state sciences. This thesis is mainly focussed on one of the M-type hexaferrites, namely barium hexaferrite. Prior to going for a review on M-type hexaferrites, we will first briefly discuss some general phenomena relevant to this thesis, like various ferroics, spin-glasses, multiferroicity and quantum paraelectrics.

1.2 Ferroics

The term “Ferroics” was coined by Aizeu to describe different types of mimetically twinned crystals in which one or more twins (also called as domains) can be switched to another equivalent state by the application of external stimulus [34]. This implies that a ferroic material is one which exists in more than one orientational state [35]. For example, in the ferromagnets, ferroelastics and ferroelectrics, the alignments of magnetic spins, strain and dipole moment can be changed to another equivalent state by applying the

conjugate magnetic, stress and electric fields, respectively. These ferroics (ferromagnets, ferroelastics and ferroelectrics) along with ferrotoroidics [36] are known as primary ferroics [36,37]. In recent years, the definition of primary ferroics has been broadened to include all types of orderings involving magnetic spins and electric dipoles such as ferromagnetism, antiferromagnetism, spin glasses, on one hand, and ferroelectricity, antiferroelectricity, dipole glasses, relaxors, on the other, as even canted antiferromagnets/antiferroelectrics and spin glasses/dipole glasses/relaxors exhibits weak magnetization, even though it does not show saturation. In this thesis, we are concerned with ordering of magnetic and electric dipoles moments only and we recapitulate a few basic definitions in the following sections.

1.3 Ferromagnetism

Ferromagnetic materials exhibit spontaneous magnetization even in the absence of external magnetic field due to parallel alignment of magnetic moments. Its direction can be reversed by the application of magnetic suitable field as revealed by the observation of a hysteresis loop in the M-H plot showing saturation of magnetization ($\pm M_s$) at higher fields exceeding the coercive field ($\pm H_c$) and remanent magnetization ($\pm M_r$) at zero field. The typical examples of ferromagnetic materials are Fe, Co and Ni [38]. As the temperature increases, the saturation magnetization (M_s) gradually decreases before disappears a critical temperature. This critical temperature is known as the Curie temperature T_c above which ferromagnetic phase transforms to the paramagnetic state where the magnetic moments are randomly oriented. The magnetic susceptibility (χ) in the paramagnetic state follows the Curie–Wiess behaviour [38]:

$$\chi(T) = \frac{C}{T - \Theta_{cw}} \qquad \ldots\ldots\ldots\ldots (1.1)$$

where C is the Curie constant and Θ_{cw} is the Curie-Wiess temperature. This behaviour is

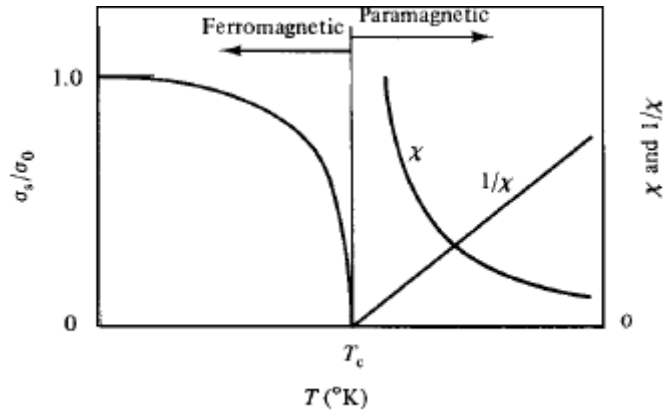

Figure 1.1: Variation of magnetization and susceptibility below and above Curie temperature (T_c) [38].

shown in Fig. 1.1. The spontaneous magnetization (M_s) is the primary order parameter for a ferromagnetic transition, which appears at T_c, continuously or discontinuously depending on whether it is a second or first-order phase transition, as a symmetry-breaking transition in the framework of Landau theory. The situation shown in Fig. 1.1 is a second-order ferromagnetic transition.

1.4 Antiferromagnetism and Ferrimagnetism

In a canonical antiferromagnetic material, the spins are aligned antiparallel to each other leading to zero spontaneous magnetization. This implies two spin sublattices, in each of which spins are arranged parallel to each other, whose net magnetization is zero. When the number of spins parallel and antiparallel to each other are not equal, as in several hexaferrites, the sublattice magnetizations do not fully cancel each other and lead to what are called ferrimagnets which may behave more or less like ferromagnets even if there are two or more magnetic sublattices [38,39]. Another variant of antiferromagnets arises for canted spins with both ferromagnetic and antiferromagnetic components transverse to each other. Such canted antiferromagnets behave like ferromagnets macroscopically with net magnetization but without saturation. There is a rich variety of

antiferromagnets with Ising and Heisenberg spins. Few examples of Ising antiferromagnets is given in Fig. 1.2. In canonical antiferromagnets, the spin moments retain their anti-parallel alignment in the presence of moderate external magnetic field also but show spin flop transition above a critical field at which all the moments get aligned in the same direction leading to double M-H hysteresis loop above a critical field $\pm H_c$. The typical examples of antiferromagnetic materials are MnO, FeO, CoO, NiO and α-Fe_2O_3 [38]. When temperature increases, the anti-parallel alignment of moments is destroyed gradually and the susceptibility increases upto a critical temperature above which it begins to decrease again as per the Curie-Wiess law in the paramagnetic phase. This critical temperature is known as Neel temperature (T_N). The variation of magnetic susceptibility of a canonical antiferromagnetic material with temperature is shown in Fig. 1.3 where the Curie Weiss temperature Θ_{cw} is on the negative temperature axis and $|\Theta_{cw}| = T_N$ in this case. In many frustrated antiferromagnets with competing ferromagnetic and antiferromagnetic interaction, $T_N << |\Theta_{cw}|$ which has been considered as a measure of frustration ($f = |\Theta_{cw}|/T_N$) [40].

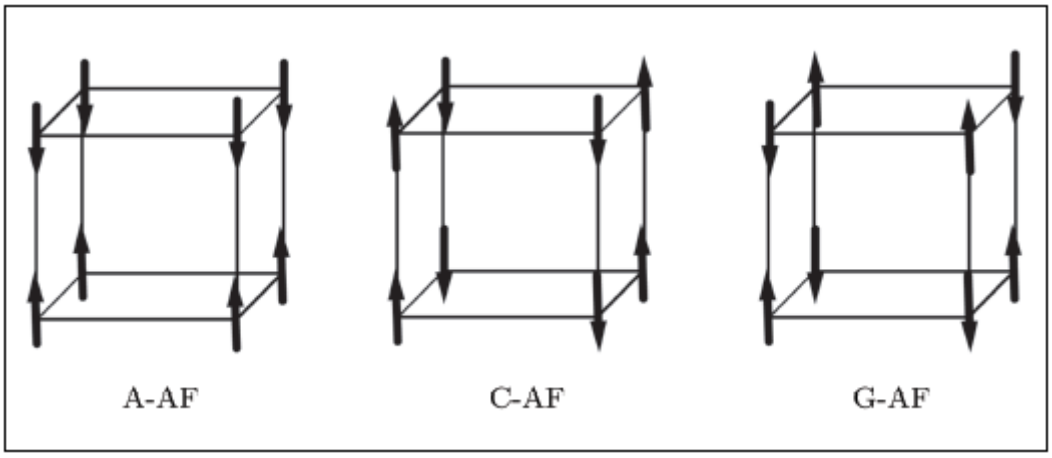

Figure 1.2: A few examples of Ising antiferromagnets [41].

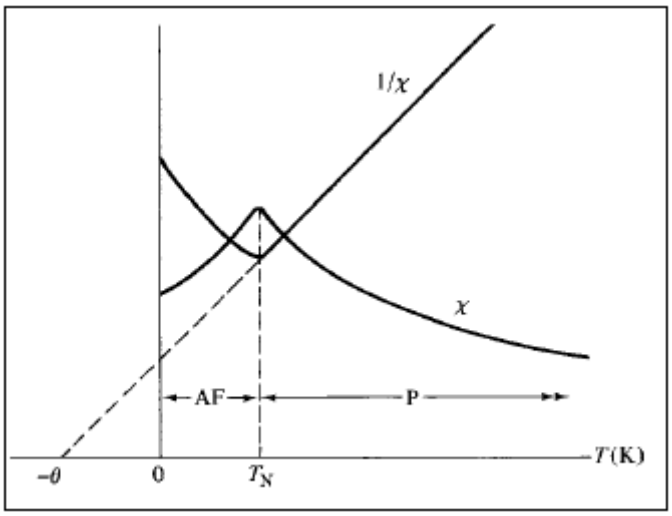

Figure 1.3: Variation of susceptibility and inverse susceptibility of an antiferromagnetic materials [38]. AF: antiferromagnetic and P: paramagnetic.

1.5 Ferroelectricity

Among the 32 crystallographic point groups, 20 of them are non-centrosymmetric and can therefore exhibit piezoelectricity, a phenomenon by virtue of which polarization and strains can be produced on application of mechanical stress and electric field, respectively, in such crystals. In piezoelectrics, the polarization/strain is linearly proportional to the stress/electric field. Even when this linearity is lost, a quadratic dependence is also present which is called as electrostriction, a phenomenon that occurs even in centrosymmetric crystals. Out of the 20 piezoelectric point groups, 10 of them have a unique polar axis [42,43]. The crystalline materials possessing a unique polar axis are known as pyroelectrics. Among the pyroelectrics, if the spontaneous electric polarization (P_S) due to alignment of dipoles in a crystallographic direction can be reversed by an external electric field, the material is said to be ferroelectric [42]. A ferroelectric material is, therefore, pyroelectric as well as piezoelectric but converse is not true.

The necessary condition for the ferroelectricity is the presence of P_S which can be reversed using external electric field in a typical P-E hysteresis [42]. The spontaneous polarization P_S in ferroelectrics may decrease with the increasing temperature and disappear continuously, as observed in order-disorder ferroelectrics like KH_2PO_4 and $KNaC_4H_4O_6$-$4H_2O$ [43–45], or discontinuously, as observed in displacive ferroelectrics like $BaTiO_3$, $KNbO_3$, $PbTiO_3$, etc. [42–45], above a critical temperature called Curie point (T_c). The Curie point (T_c) is equal to Curie-Weiss temperature Θ_{cw} for second-order phase transitions unlike $\Theta_{cw} < T_c$ for first-order phase transitions. The phase above T_c is known as non-polar paraelectric phase, in analogy with paramagnets though this analogy is not exact for displace ferroelectrics like $BaTiO_3$ [43–45]. The transition from the paraelectric phase to ferroelectric phase is accompanied with a macroscopic symmetry breaking at $T \leq T_c$ and appearance of the order parameter P_s. Further, the temperature-dependent dielectric permittivity ($\varepsilon(T)$) shows a sharp peak at the paraelectric to ferroelectric transition temperature and follow the usual Curie-Weiss law in the paraelectric state [42,43]:

$$\varepsilon(T) = \frac{C}{T - \Theta_{cw}} \qquad \ldots\ldots\ldots\ldots (1.2)$$

where C is the Curie constant and Θ_{cw} is the Curie-Weiss temperature.

1.6 Antiferroelectricity and Ferrielectricity

In analogy with antiferromagnetic materials, canonical antiferroelectrics possess antiparallel electric dipole moments of equal magnitude. This arrangement of dipole moments leads to zero spontaneous polarization. $PbZrO_3$, $NaNbO_3$ and $PbHfO_3$ are a few examples of antiferroelectric materials [42–45]. Macroscopic polarization can be induced in these materials by the application of high electric field as a result of a switching of all the dipoles in the field direction at high fields. This leads to a double hysteresis loop

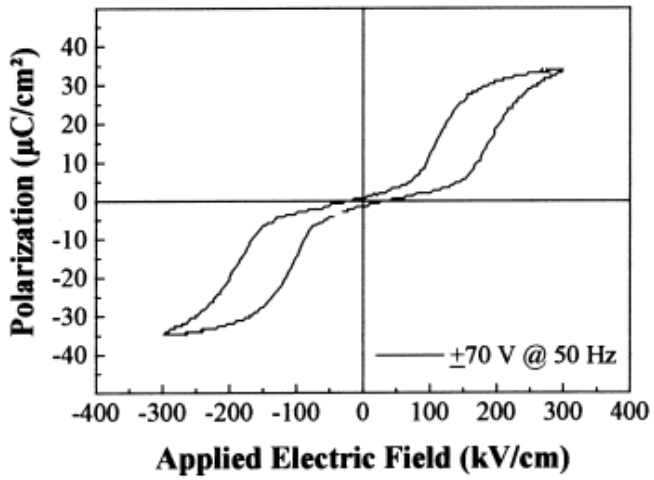

Figure 1.4: Typical hysteresis loop for an antiferromagnetic material [46].

characteristic [44] as shown in Fig. 1.4. With increasing temperature, these materials show antiferroelectric to paraelectric transition at a critical temperature (T_N) commonly known as Neel transition temperature, in analogy with antiferromagnets, at which the dipoles disappear/randomise in displacive/order-disorder systems. In the paraelectric state, the dielectric constant follows the Curie-Wiess law, usually with negative value of Curie-Wiess temperature (Θ_{cw}) in canonical antiferroelectrics.

When there are unequal number of electric moments in antiparallel directions or if the dipole moments are of unequal magnitude, they may lead to a ferrielectric state as shown in Ca^{2+} doped $SrTiO_3$ [47] and $NaNbO_3$ substituted $CaTiO_3$ [48].

1.7 Quantum Paraelectrics

The term 'Quantum Paraelectric' was coined by Muller and Burkard [49] to explain the low-temperature saturation behaviour of the dielectric constant of incipient ferroelectric materials whose paraelectric state gets stabilized down to the lowest temperatures due to quantum fluctuations. A typical behaviour of the dielectric constant in the quantum paraelectric state is shown in Fig. 1.5 for a canonical system $SrTiO_3$. In the high-temperature region of the paraelectric state, dielectric constant follows the usual

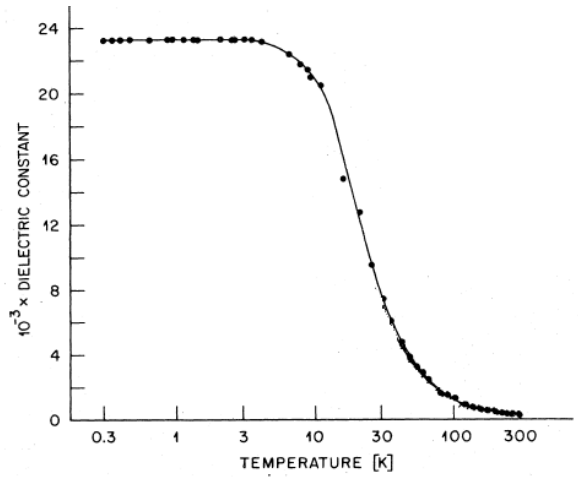

Figure 1.5: Variation of dielectric constant with temperature for a quantum paraelectric [49].

Curie-Wiess law with decreasing temperature but deviates at intermediate temperatures and then saturates at low temperatures. The saturation behaviour of the dielectric constant was explained in terms of Barrett's law [49,50], which is the quantum-mechanical analogue of the classical Curie-Weiss law:

$$\varepsilon(T) = \frac{C'}{\frac{1}{2}T_1 \coth(\frac{T_1}{2T}) - T_0}, \qquad \ldots\ldots\ldots\ldots (1.3)$$

where T_0 is analogous to the Curie-Wiess temperature (Θ_{cw}). The positive and negative signs of T_0 correspond to the presence of ferroelectric and antiferroelectric type correlations among the dipoles. T_1 is the temperature below which the quantum effects start affecting the dipole ordering. C' is related with electric dipoles density similar to Curie constant C. For $T > T_1$, the first term in the denominator of Equation (1.3) asymptotically approaches T and the Barret's law is reduced to Curie-Weiss law [51]. $SrTiO_3$ [49], $KTaO_3$ [52,53], $CaTiO_3$ [54] and $NaNbO_3$ [55] are a few examples of quantum paraelectric materials, where $SrTiO_3$ and $KTiO_3$ have got positive T_0 while $CaTiO_3$ and $NaNbO_3$ show negative T_0. The quantum fluctuations in such quantum

paraelectrics can be suppressed by applying external electric field, pressure/stress and/or chemical substitutions [52,56].

1.8 Spin-Glasses, Dipole glasses and Relaxors

Spin glasses are a class of magnetic materials in which the spins freeze in a random direction below a characteristic critical temperature at which the spin glass freezing dynamics shows divergence as a result of ergodic symmetry breaking [57–61]. Theoretically, this transition has been shown to be a thermodynamic phase transition for canonical spin glasses [57]. It has two main ingredients, frustration and random disorder. The frustration effect can be understood by considering a triangular lattice as shown in Fig. 1.6. It is evident from Fig. 1.6(a) that if all the nearest neighbour interactions are ferromagnetic, the Ising spins can order ferromagnetically in the same direction. On the other hand, if the nearest neighbour interactions are antiferromagnetic, the antiferromagnetic ordering gets frustrated as illustrated in Fig. 1.6(b). This may result in large degeneracy of the ground state. The first spin-glass transition was reported in the alloy systems in which the magnetic ions in dilute concentration are randomly distributed

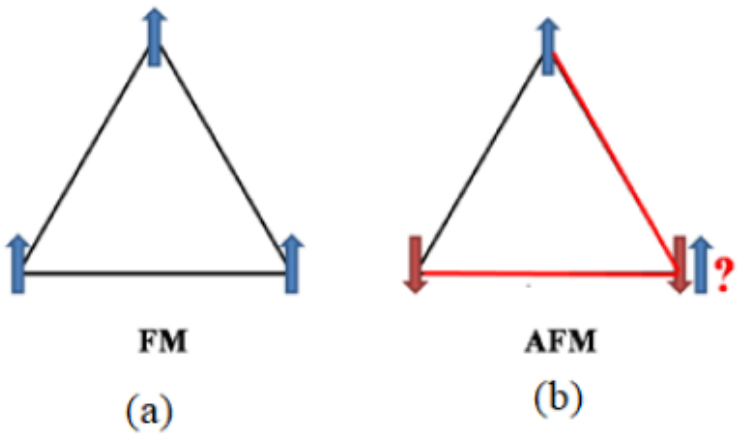

Figure 1.6: Schematic representation of magnetic spin in triangular lattice by considering (a) ferromagnetic and (b) antiferromagnetic nearest neighbour interactions [62].

in a non-magnetic metal host lattice [57]. The examples of canonical (dilute) spin glasses are CuMn, AuFe, AgMn etc. [57,60,61]. The spin glasses exhibit several characteristic features as listed below:

(1). Spin glasses are known to show history-dependent bifurcation/irreversibility of zero-field cooled (ZFC) and field cooled (FC) magnetization (M(T)) at a characteristic temperature called T_{irr} with a peak in the ZFC M(T) curve called spin-glass freezing temperature (T_f). In canonical spin glasses, T_{irr} nearly coincides with the T_f while in concentrated systems (leading to cluster glasses) $T_{irr} > T_f$ [60,61]. Fig. 1.7 depicts the temperature dependence of ZFC and FC M(T) curves for dilute magnetic alloy system CuMn showing history-dependent bifurcation [61].

(2). Spin glasses exhibit frequency dispersion across the spin-glass freezing temperature T_f in the ac susceptibility plots with $T_f(\omega)$ shifting to higher temperature side with

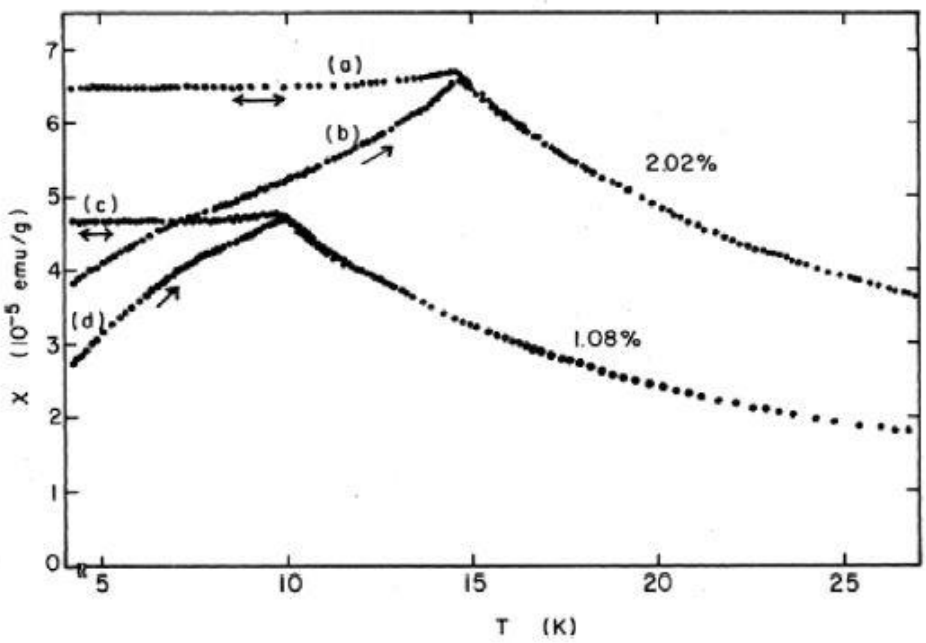

Figure 1.7: Static (dc) susceptibility (M/H) vs temperature (T) plots of CuMn system with different magnetic impurity concentration (Mn) [61].

increasing frequency. The $T_f(\omega)$ has been modelled using Vogel-Fulcher and power-law type critical dynamics with a critical Vogel-Fulcher freezing temperature (T_{VF}) and spin-glass transition temperature (T_{SG}), respectively, at which the slowest spin dynamics diverges as a proof of ergodic symmetry breaking [57–61]. The temperature dependence of the real part of ac susceptibility of the classical CuMn system for different frequencies are illustrated in Fig. 1.8 where the peak temperature shifts to higher temperature side with increasing frequency of measurement.

(3). The thermodynamic nature and the critical behaviour of spin glasses is discussed not only in terms of dc and ac susceptibility studies with history-dependent irreversibility and ergodic symmetry breaking, respectively but also in terms of divergence of the non-linear susceptibility (χ_3 and χ_5) [57–61]. Fig. 1.9 illustrates the comparison of the temperature dependence of various harmonics for the long-range ordered ferromagnetic and spin glass systems [63].

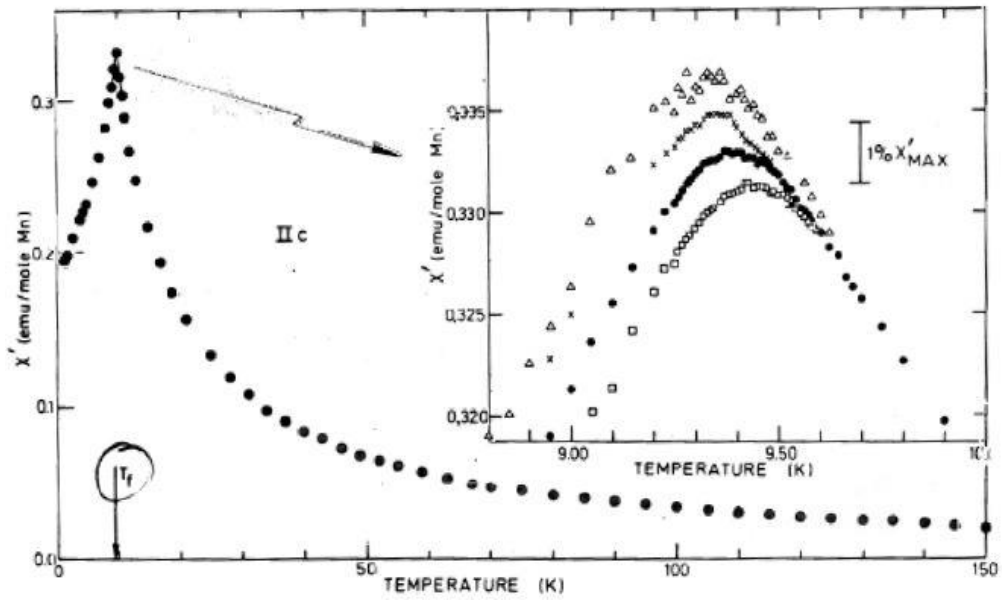

Figure 1.8: The temperature dependence of real part of ac-susceptibility of CuMn alloy system. Inset shows frequency dispersion across the freezing temperature. Peak position shifts to higher temperature side with increasing frequency [61].

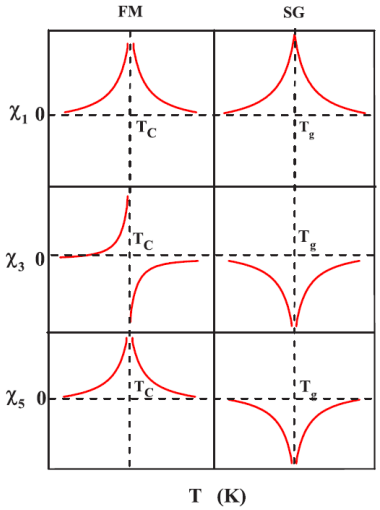

Figure 1.9: Schematic representation of the temperature variations of the odd harmonics (χ_1, χ_3 and χ_5) in ac susceptibility [63].

(4). In spin glasses, the spin-glass freezing temperature T_f shifts to lower temperature side with increasing field and $T_f(H)$ falls on either de Almeida-Thouless (A-T) or Gabay-Toulouse (G-T) lines in the T-H plane with characteristic exponents [64–68]. The Ising and Heisenberg spins may respond differently to magnetic field.

(5). Spin-glass phase well below T_{VF}/ T_{SG} exhibits very slow spin dynamics which has been verified by the relaxation of (i) thermoremanent magnetization (TRM) or (ii) isothermal remanent magnetization (IRM) with time (t) [69–74]. Fig. 1.10 depicts a typical time evolution of TRM curve which shows a stretched exponential behaviour due to distribution of relaxation times as results of multi-valleyed ground state of spin glasses [57–61].

(6) The spin glasses are also known to exhibits memory and rejuvenation effects in the spin-glass state. In case of interacting clusters of spins, as observed in concentrated systems near the percolation threshold, one observes what is called as cluster glass freezing, as distinct from atomic canonical spin glasses like CuMn systems [60,61]. The characteristic (1) and (5) are common to both cluster spin glasses and superparamagnetic

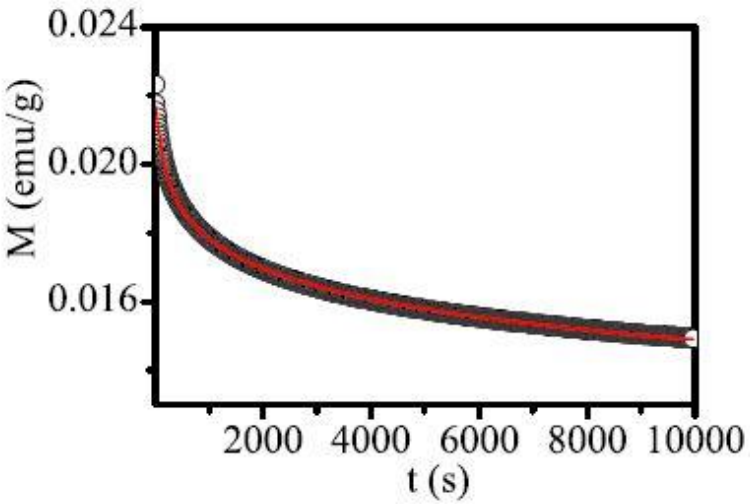

Figure 1.10: Thermoremanent magnetization (TRM) plot of $Ca(Fe_{1/2}Nb_{1/2})O_3$ recorded at 15 K for 1000 Oe applied magnetic field using wait time of 1000 s [75].

(SPM) systems where non interacting clusters of spins as in SPM or interacting clusters relax with decreasing temperature as well as a function of time at a fixed temperature. The spin-glass freezing and superparamagnetic blocking transitions can be distinguished by using criterion (2) and (3) above.

In analogy with atomic spin glasses where there is dilute concentration of magnetic impurity in non-magnetic host, there are several incipient ferroelectrics like $KTaO_3$, which on doping with very small concentration of smaller size ion like Li^{1+} at K^{1+} site induces a local dipole moment. Such dipoles even in dilute concentration, have been shown to undergo freezing similar to spin glasses in some respects [52,76] and such frozen states are typically termed as dipole glasses. Dipole glass behaviour has been shown in a completely neutral matrix-like KCl also, unlike highly polarizable incipient ferroelectrics like $KTaO_3$, at very low temperatures due to random site dipoles induced by Li^{1+} doping [76].

Relaxor ferroelectrics also exhibit frequency dispersion of dielectric constant around a peak temperature T_f with very diffuse $\varepsilon(T)$ response. The peak temperature

$T_f(\omega)$ shows characteristic frequency and electric field dependence similar to dipole glasses with one significant difference. Unlike dipole glasses and spin glasses, it is possible to induce ferroelectric state in relaxor ferroelectrics below the critical Vogel-Fulcher freezing temperature. The best example of relaxor ferroelectrics is $Pb(Mg_{1/3}Nb_{2/3})O_3$ [77–79] which with 10% $PbTiO_3$ substitution shows not only critical freezing at T_{VF} but also a ferroelectric phase below T_{VF} in E -T diagram [80] above a critical field.

1.9 Multiferroics

Multiferroic materials exhibit atleast two primary ferroicity (ferromagnetism, ferroelectricity, ferroelasticity and toroidicity) in the same phase [36,37,89,90,81–88] with coupling between the respective order parameters (M, P and strain). This definition of multiferroicity has in recent decades been broadened to include antiferroelectrics, antiferromagnets, spin glasses and dipole glasses/relaxors as some of them do show coupling of diverse order parameters [84]. Magnetoelectric multiferroic materials have strong potential in the designing of multifunctional sensors and actuators as well as various spintronic and storage devices [84,90]. Multiferroic materials are broadly classified into two categories type I and type II depending on whether they exhibits two or only one primary order parameter [85,87]. In Type I magnetoelectric multiferroics, the magnetization (M_s) and ferroelectric polarization (P_s) are primary order parameters which emerge below magnetic (T_N) and ferroelectric (T_c) transition temperatures, separately while in type II multiferroics, the ferroelectric polarization (P_s) is a secondary order parameter which emerges from specific arrangement of spins that appear below a critical temperature with only one primary order parameter [84,85,96,86,87,89,91–95]. The typical examples of type I multiferroics is $BiFeO_3$ (T_c ~ 1103 K, T_N ~ 643 K, P_s ~ 100$\mu C/cm^2$) while that of type II is $TbMnO_3$ (T_c ~ 28 K, T_N ~ 41 K, P_s ~ 10^{-2} $\mu C/cm^2$).

1.10 The Hexaferrites

In this section, we present a brief background on the hexaferrites with emphasis on their crystal structure, multiferroics behaviour, their applications and quantum mechanical phenomena.

1.10.1 Crystal Structure

Hexaferrites are basically ferrites with hexagonal or rhombohedral structures, both of which are described using a hexagonal unit cell. They are broadly classified as M, Y, W, Z, X and U types [11,12]. The chemical formulae for the different type of hexaferrites are listed in Table 1.1 while their position in the pseudo ternary composition phase diagram is shown in Fig. 1.11. In the Phase diagram, 'A' could be a divalent cation, such as Ba^{2+}, Sr^{2+}, Pb^{2+}, Ca^{2+} etc, whereas Me could be a transition metal cation (Sc, Ti, Cr, Mn, Co, Fe etc.) or combination of these cations with trivalent cations such as Al^{3+}, In^{3+} etc. In principle, one can design an infinite variety of hexaferrites by choosing AO, MeO, and Fe_2O_3 in different proportions leading to different stacking of the R, S and T

Table 1.1: Chemical formula, sequences of S, R, and T blocks, and space groups for different type of hexaferrites [12].

Hexaferrites	Chemical Formula	Sequence of the R, S and T Blocks	Space Group
M	$AFe_{12}O_{19}$	RSR* S*	$P6_3/mmc$
W	$AMe_2Fe_{16}O_{27}$	SSRS*S*R*	$P6_3/mmc$
X	$A_2Me_2Fe_{28}O_{46}$	SRS*S*R*	R3m
Y	$A_2Me_2Fe_{12}O_{22}$	STSTST	R3m
Z	$A_3Me_2Fe_{24}O_{41}$	STSRS*T*S*R*	$P6_3/mmc$
U	$A_4Me_2Fe_{36}O_{60}$	SRS*R*S*T*	R3m

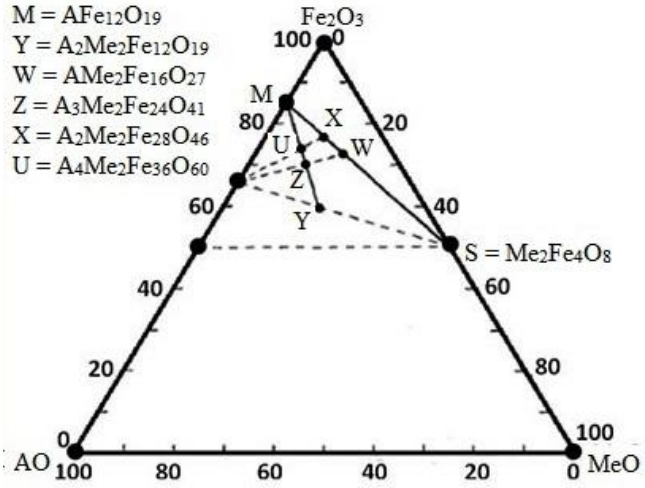

Figure 1.11: Ternary phase diagram for the hexaferrites.

fundamental building blocks. Accordingly, all these hexaferrites have nearly similar "a" and "b" lattice parameters of the hexagonal unit cell but differ in the c-parameter due to different stackings, akin to polytypes in SiC [97]. The different hexaferrites have considerably different physical properties.

The M-type hexaferrites have a complex crystal structure [12]. To understand its crystal structure, we consider a hexagonal closed packed layer of oxygen labelled as A-layer in Fig. 1.12. It is evident from the figure that the next oxygen layer can be placed in two different ways (B or C) for close packing. When the oxygen ions are placed at downward and upward triangular sites shown in the A-layer, the resulting layers are labelled as B and C layers, respectively. In two dimensions, each layer has got a rhombic unit cell as shown for the A-layer in the figure. If the A-sites are at the origin (0, 0), the B and C sites acquire (1/3, 2/3) and (2/3, 1/3) positions in the unit cell along the face diagonal A2A4 in Fig. 1.12. The stacking of A, B and C type layers such that no two neighbouring layers are identical leads to different periodicities whose hexagonal "a" and

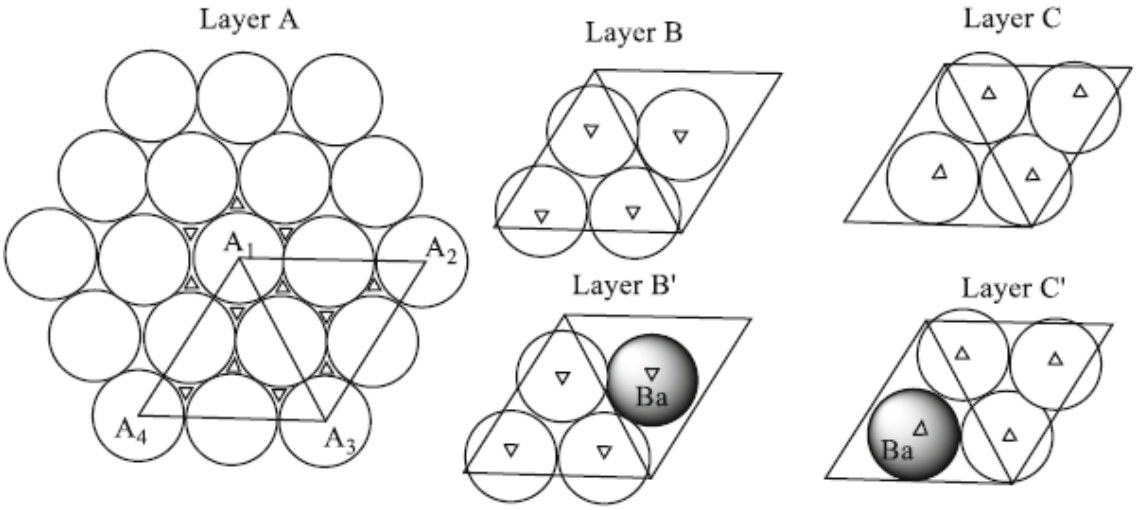

Figure 1.12: The arrangement of the different layers of O^{2-} and Ba^{2+} ion within the unit cell of $BaFe_{12}O_{19}$ M-type hexaferrite [98].

"b" lattice parameters are equal while c-parameter is an integral multiple of the layer thickness. In M-type hexaferrite, one of the oxygens is replaced by an alkaline earth metal ion such as Ba^{2+} or Sr^{2+} to form a B' and C' layers. These layers A, B, C and B' and C' are arranged in the AB'ABCAC'ACB manner in M-type hexaferrites as shown in Fig. 1.13. The trivalent transition metal ions, which are much smaller in size with respect to M and O ions, occupy the octahedral, tetrahedral and trigonal bipyramid void sites [11,12].

There is another approach to understand the crystal structure of hexaferrites using S, R and T blocks [11,12]. These blocks behave as the fundamental structural blocks and any type of hexaferrite can be obtained by arranging the S, R and T blocks in different sequences and proportions. The general chemical formula for the S, R, and T blocks are $[Me_2^{2+}Fe_4^{3+}O_8]$ or $[Fe_6^{3+}O_8]^{2+}$, $[Me^{2+}Fe_6^{3+}O_{11}]^{2-}$, and $[A_2^{2+}Fe_8^{3+}O_{14}]$, respectively. The S block contains two close-packed layers of oxygen ion in the cubic environment, R block consists of three close-packed layers of oxygen ions in hexagonal (ABA) environment in which one oxygen ion in the middle layer is replaced with A^{2+} ion while T block consists

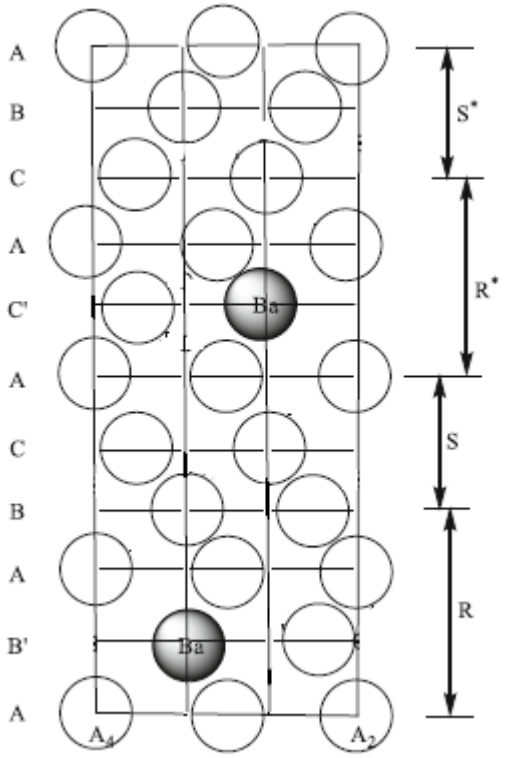

Figure 1.13: Unit cell of $BaFe_{12}O_{19}$ [98].

of four hexagonal close-packed layers of oxygen ions in which one oxygen ion in the two middle layer is replaced with A^{2+} ion as shown in Fig. 1.14. These fundamental blocks contain three different types of interstitial positions, named tetrahedral (TH), octahedral (OH) and trigonal bipyramidal (TBP) [11,12]. Within the unit cell, the transition metal cations like Fe^{3+} occupy these interstitial positions.

The unit cell of the M-type hexaferrites contains cubic closed packed S block and hexagonal closed packed R block in the sequence SRS*R*, as shown in Fig. 1.13, where the layers with asterisk (*) represent the same blocks rotated by 180^0 about the hexagonal axis with respect to the initial block without asterisk. The sequence SRS*R* leads to the hexagonal structure with space group $P6_3/mmc$ for the nuclear structure of M- type hexaferrites like $BaFe_{12}O_{19}$, which is the subject matter of investigation in this thesis. In a similar way, one can generate the stacking sequence in the unit cell of other hexaferrites

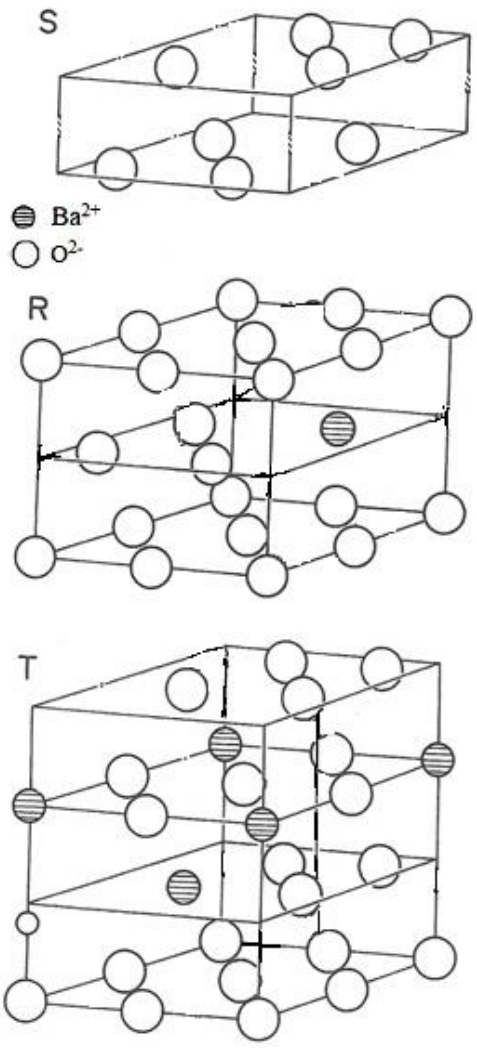

Figure 1.14: S, R and T blocks [12].

illustrated in Table 1.1. For example, the unit cell of Z-type hexaferrites corresponds to STSRS*T*S*R* sequence. Among the various hexaferrites containing proper sequencing of these three fundamental blocks shown in Table 1.1, X, Y and U type have rhombohedral R3m space group while others have $P6_3/mmc$ space group. Both the structures are referred to hexagonal unit cell as per the convention.

1.10.2 Multiferroicity in Hexaferrites

The basic magnetic structure of hexaferrites is believed to be collinear ferrimagnetic type as per the classic Gorter model [39]. But this magnetic structure changes to longitudinal conical, spiral or screw-type either due to chemical substitution

with a foreign ion or with decrease in temperature itself without any chemical substitution [3,29,99–102]. Among the various type of hexaferrites, the multiferroic behaviour was first explored on Y-type hexaferrite with $Ba_{0.5}Sr_{1.5}Zn_2Fe_{12}O_{22}$ composition [103]. Later on, multiferroic properties were discovered in other type of hexaferrites, mostly as a results of chemical substitutions in M, Y, Z and U-type also [1,2,104,105,4–6,29,89,91,94,103].

To understand the origin of multiferroicity in hexaferrites, we consider Y-type hexaferrite $Ba_2Mg_2Fe_{12}O_{22}$ (BMFO), as an example, whose magnetic structure changes from collinear to noncollinear with decreasing temperature [101,106–108]. BFMO undergoes paramagnetic to collinear ferrimagnetic transition at 553 K [106] with collinear magnetic structure which changes to proper a screw-type below 195 K and eventually turns into longitudinal conical structure below 50 K [101,106,109,110]. These non-collinear helical magnetic structures are usually explained in terms of 'S' and 'L' blocks of spins representing the net magnetic moment in each block, rather than each R, S, and T structural blocks [101]. The collinear, screw and longitudinal conical magnetic structures of BMFO are shown in Fig. 1.15 in terms of the 'S' and 'L' block moments. The origin of the spontaneous polarization in BMFO can be explained using inverse Dzyaloshinskii-Moriya (DM) effect (spin-current model) [111]. The net polarization is given as [111]:

$$P = a \sum_{i,i+1} e_{i,i+1} \times (S_i \times S_{i+1}), \qquad \ldots\ldots\ldots\ldots (1.4)$$

where a is a constant and $e_{i,i+1}$ is a unit vector in the direction of the propagation vector k connecting the two adjacent blocks with spins S_i and S_{i+1} and hence the corresponding moments. First, we apply this model to collinear structure with all spins in the ab plane, as shown in Fig. 1.15(a). For this structure, the cross product of adjacent spins S_i and S_{i+1} in the S and L blocks leads to another vector $Js \sim (S_i \times S_{i+1})$ which is zero. So, there is no magnetic structure-driven ferroelectric polarization in this case and hence such a structure

is not multiferroic. Similarly, proper screw-type magnetic structure, shown in Fig. 1.15(b), also gives zero polarization. For the longitudinal-conical magnetic structure (see Fig. 1.15(c)). The longitudinal component parallel to the c-axis, which is the propagation vector, gives collinear type magnetic structure while the transverse component perpendicular to the c-axis gives proper screw type structure. Both the collinear and proper screw-type spin structures lead to zero polarization as per Equation (1.4) and

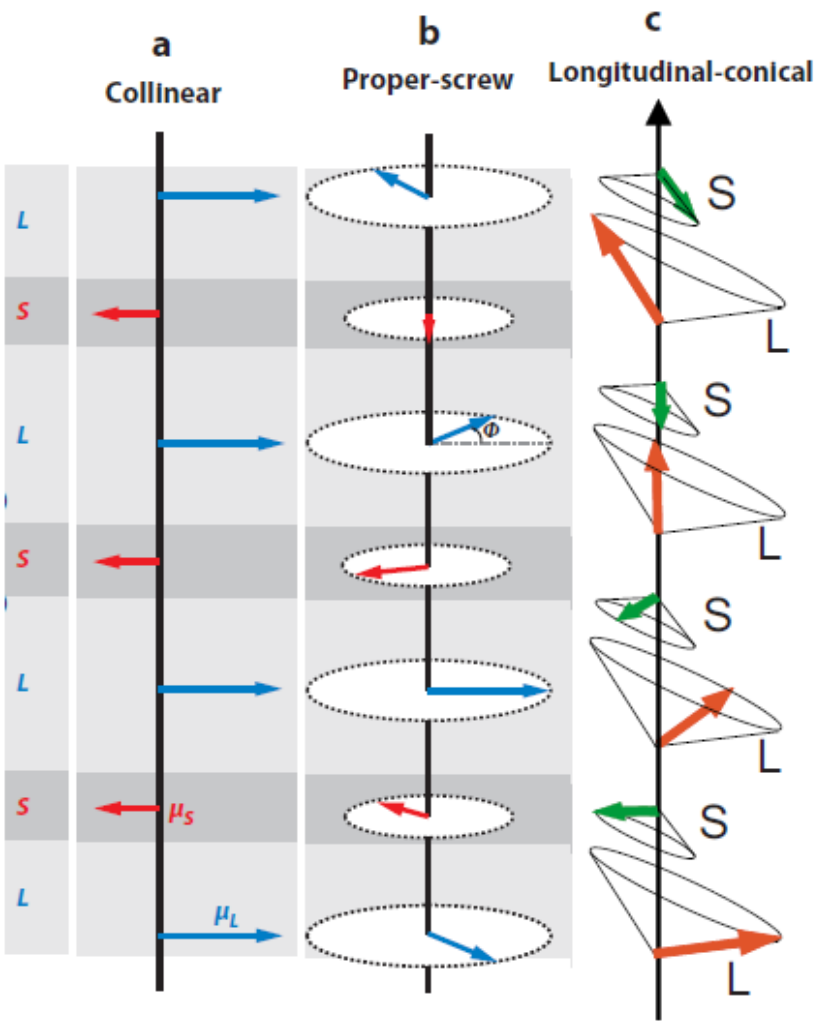

Figure 1.15: Schematic proposed magnetic structures of magnetoelectric Y-type hexaferrites. (a) collinearly ferrimagnetic [96], (b) the proper-screw [96] and (c) longitudinal-conical [101] magnetic structure. The short and long arrows indicate the effective moment in S and L blocks, respectively [96,101].

hence longitudinal conical structure also leads to zero polarization. Application of a magnetic field (H) less than 0.1 T in the transverse direction, i.e., perpendicular to the c-axis, leads to a transverse-conical structure as shown in Fig. 1.16 [101]. The longitudinal components parallel to the c-axis form a cycloidal type structure shown in Fig. 1.16(b) while the transverse components give collinear magnetic structure shown in Fig. 1.16(a). As discussed earlier, collinear structure gives zero polarization but the cycloidal spin components give finite polarization as per Equation (1.4). However, increasing the field

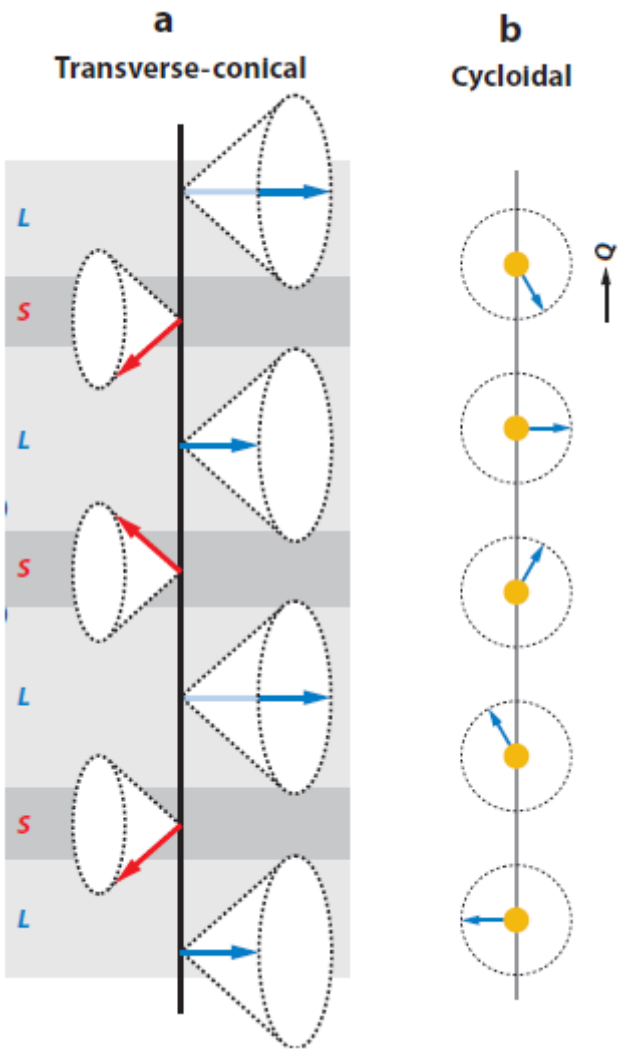

Figure 1.16: Schematic (a) proposed transverse-conical [101] magnetic structures of Y-type hexaferrites and (b) cycloid type magnetic structure [96].

strength results in a non-collinear to a collinear type change of magnetic structure with zero polarization [96]. The ferroelectric state of BMFO induced by magnetic field shows very large polarization ~ 90 μCm^{-2} at 5 K [112]. On the basis of the conical magnetic structure of hexaferrites, high-temperature multiferroic behaviour has been explored in Z-type hexaferrites $(Sr,Ba)_3Co_2Fe_{24}O_{41}$ [1,3,4,9,113–116] and M-type ferrites $BaSc_xFe_{(12-x)}O_{19}$ [29].

1.10.3 Technological Applications of Hexaferrites

Among the most used magnetic materials are ferromagnetic metals and alloys and ferrimagnetic ceramics. The hexaferrites are used as permanent magnets which have numerous technological applications relevant to commercial section. For example, these magnets are frequently used in motors, transformers, generators, mobile communications, actuators and sensors, defence and aerospace structures, information storage and transport [11–13,117]. Other applications of hexagonal ferrites are illustrated in Fig. 1.17 schematically to give a sense of the importance of hexaferrites as important magnetic materials [12]. We elaborate a few applications of hexaferrites in different fields in the following.

Permanent Magnets (PMs)

The best permanent magnets use alloys of rare-earth metals Nd, Pr and Dy. But due to limited resources these rare earth metals, their cost is very high. As a cheaper alternative, M-type hexaferrites (especially $BaFe_{12}O_{19}$ and $SrFe_{12}O_{19}$) are commonly used for applications as permanent magnets. Hexagonal ferrites as permanent magnets are frequently used in loudspeakers, electrical motors, relays, correction magnets in the cathode ray tubes, clocks, dynamos, refrigerators, and sensors and motors in automobiles and microphones [12]. But there are applications like wind turbines where hexaferrites have not been able to replace rare earth metal alloys-based magnets. Due to cheaper cost,

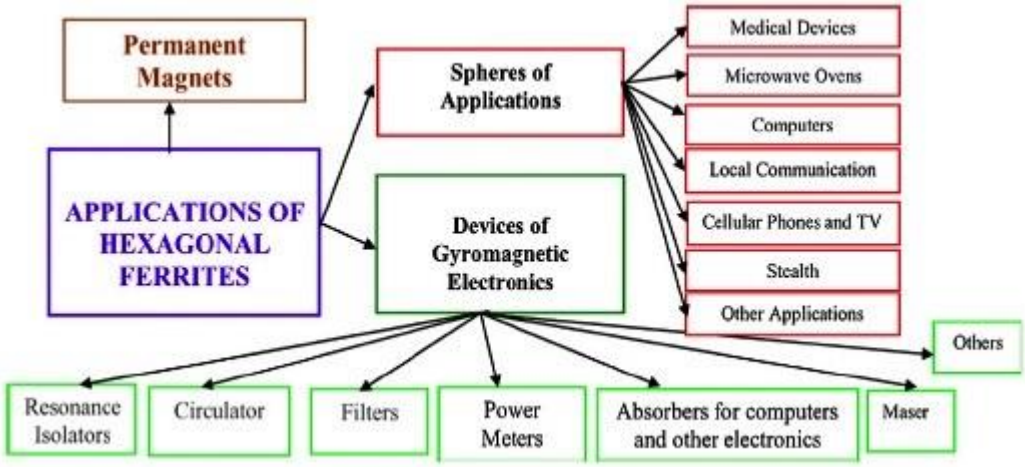

Figure 1.17: Practical applications of hexagonal ferrites [12].

ease of synthesis and fabrication any shape, the hexaferrites have replaced expensive rare earth alloys in majority of applications as permanent magnets [12].

Plastoferrites

In plastoferrites, sintered powder of M-type hexaferrites are dispersed into a resin or a thermoplastic matrix [12]. Such composite magnetic materials are not brittle and hard to break. They can also be cut and shaped in any complex shape easily.

Electrical and Microwave (MW) Devices

Microwave spectrum of the hexagonal ferrites in the 1 to 110 GHz region makes it useful for applications in radars, mobile phones, wireless communication, fixed telecoms, space and astronomy research equipment and aerospace applications [117].

1.11 Recent Advances in M-type Hexaferrites

This thesis is mainly focussed on one of the M-type hexaferrites, namely $BaFe_{12}O_{19}$. This section presents a brief overview of crystal structure, magnetic structure, magnetic transitions, quantum phase transitions and multiferroic behaviour of M-type hexaferrites.

Crystal (Nuclear) Structure

The M-type hexaferrites are isomorphous with the mineral magnetoplumbite $PbFe_{7.5}Mn_{3.5}Al_{0.5}Ti_{0.5}O_{19}$ because of identical crystal structure with hexagonal space group $P6_3/mmc$ [12,117]. The asymmetric unit of M-type hexaferrite contains 11 different Wyckoff positions where Ba/Sr/Pb ions occupy 2d site, Fe ions occupies 2a, 2b, 4f1, 4f2 and 12k sites while oxygen ions occupy 4e, 4f, 6h, 12k and 12k sites [118,119]. The location of the Fe^{3+} at 2b Wyckoff site which is pentacoordinated within TBP is unusual for close packing and has attracted enormous attention and remains controversial even at present [15,119–127]. The Fe^{3+} at 2b site is shown schematically in Fig. 1.18. In the average nuclear structure of M-type hexaferrites, Fe^{3+} is assumed to occupy a position at the mirror plane perpendicular to the c-axis. The TBP coordination consists of two inverted tetrahedra as can be seen from Fig. 1.18. Various studies on the crystal structure using X-ray diffraction [119,120,123], neutron diffraction [15] and Mössbauer spectroscopy [121,122,124–127] reveal that the magnetic Fe^{3+} ion at the centre of the TBP, in fact, oscillates between the two 4e Wyckoff sites with a very high frequency such

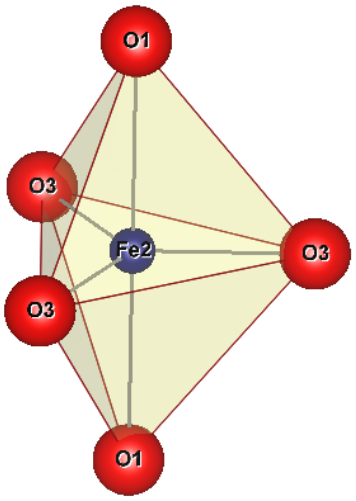

Figure 1.18: Trigonal bipyramid polyhedra

that the time and space averaged position of Fe^{3+} appears to be at the mirror plane passing through the middle of the TBP perpendicular to the c-axis. It has also been proposed that this dynamics may freeze at one of the two possible positions below 4 K randomly [15]. In case of $BaFe_{12}O_{19}$, it has been shown through simulation studies that due to a delicate balance between short-range Pauli repulsion and long-range Coulomb interaction, an off-center displacement of Fe^{3+} ion may occur within the FeO_5 bipyramid [14]. Further, on the basis of phonon mode analysis of $BaFe_{12}O_{19}$ and first-principles calculations, it has been predicted that the nonpolar space group $P6_3/mmc$ of $BaFe_{12}O_{19}$ may change to a polar $P6_3mc$ below 3 K under external stress [16,128].

Magnetic Structure

Magnetic structure of M-type hexaferrites is very complex with as many as 12 Fe^{3+} ions occupying three different coordinations, namely tetrahedral (TH), octahedral (OH) and trigonal bipyramid (TBP), of oxygen ions occupying five different crystallographic sites 2a (OH), 2b (TBP), $4f_{iv}$ (TH), $4f_{vi}$ (OH), and 12k (OH) [39]. Based on an excellent agreement between the calculated saturation magnetization and the experimental value of 40 μ_B per unit cell, Gorter [39] proposed a collinear magnetic structure of $BaFe_{12}O_{19}$. According to this model, all the $3dFe^{3+}$ spins are Ising type with the spins at the 2a, 2b and 12k sites being all up while the spins at the $4f_1$ and $4f_1$ sites being all down along the c-axis. Later, Bertaut et. al. [129] proposed three different magnetic models (including the Gorter model) for the magnetic structure of M-type hexaferrites. These models are summarised in Table 1.2. Subsequent symmetry analysis along with the analysis of the neutron diffraction patterns revealed that the magnetic spins are arranged according to the magnetic space group $P6_3/mm'c'$ with propagation wave vector k = (0,0,0) as per model-I, which is the Gorter model [130,131]. Experimental studies reveal that substitution of the magnetic or non-magnetic cations or

Table 1.2: magnetic models for M-type hexagonal ferrites

Magnetic sites	Model –I	Model –II	Model -III
2a	↑	↓	↓
2b	↑	↓	↓
$4f_{iv}$	↓	↑	↓
$4f_{vi}$	↓	↓	↑
12k	↑	↑	↑

co-substitutions with elements such as Mn, In, Sc, (Co, Ti), (Mg, Ti), and (Ir, Co) at the magnetic sites may lead to conical [29,102,132–136] and helicoidal antiphase spin orderings with non-collinear magnetic structures [132,133]. Kalvoda et al. [136] have, however, suggested that $BaFe_{12}O_{19}$ may have a canted magnetic structure even without any substitution but no experimental evidence was ever published for such a canted spin configuration.

Magnetic Phase Transitions

Based on dc susceptibility measurements on $BaFe_{12}O_{19}$ single crystals along and perpendicular to the c-axis, Chen et at. [137] proposed the existence of two magnetic transitions at ~ 80 K and ~ 55 K along and perpendicular to the c-axis, respectively, as shown in Fig. 1.19. However, these transitions are very broad and the location of the actual transition temperatures may not be exact. Raman scattering studies on single crystals of $BaFe_{12}O_{19}$ by Hein et al. [138] suggest two magnetic transition around ~ 80 K and ~ 200 K based on the anomalies in the temperature dependence of the integrated intensities of the magnon peaks observed by Raman scattering. It was argued that strong spin fluctuations persist above 200 K. McCloy et al. [139] studied the ac susceptibility $\chi'(\omega, T)$ as a function of temperature (T) and frequency (ω) of the nano- and

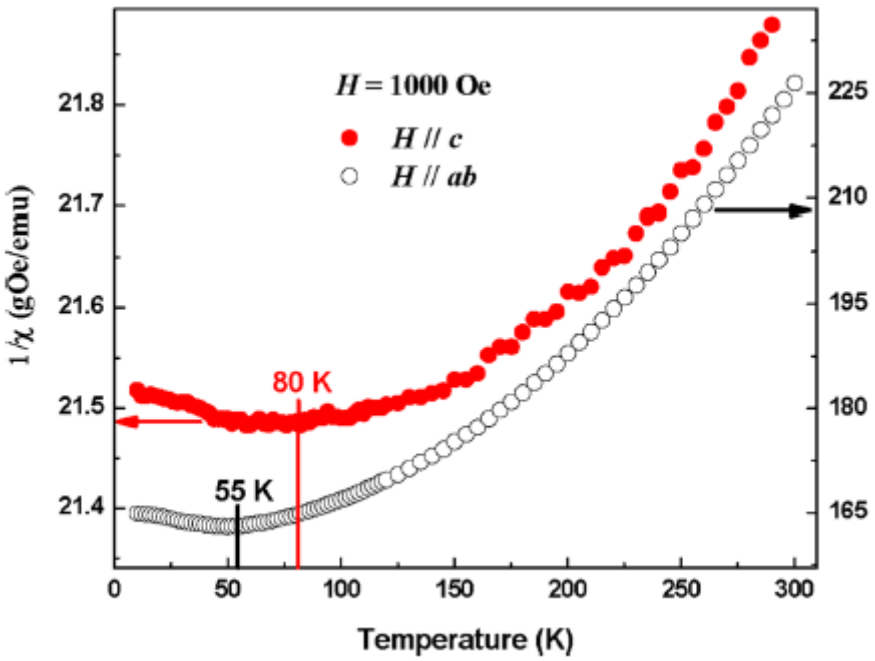

Figure 1.19: Temperature dependence of reciprocal susceptibility of $BaFe_{12}O_{19}$ single-crystal measured with dc field of 1000 Oe applied parallel (H // c) and perpendicular (H // ab) to the c-axis [137].

micro-meter sized commercial powders of $BaFe_{12}O_{19}$ and observed frequency dispersion with a peak around 50 K and 125 K in the two types of samples, respectively. But no visible shift in the peak position was reported and no analysis of the $\chi'(\omega, T)$ data was presented in this work. Barinov et al. [140] investigated the effect of mechanical milling on the magnetic behaviour of $BaFe_{12}O_{19}$ powders using Mössbauer and dc magnetisation studies. According to these workers, the room temperature magnetization of $BaFe_{12}O_{19}$ decrease rapidly after short milling time and the sample becomes almost paramagnetic at room temperature for milling times. Such sample reveal a bifurcation of ZFC and FC magnetization curves which was attributed to a spin-glass transition around 150 K. However, there was no evidence for such a transition in the unmilled $BaFe_{12}O_{19}$ powder. In the chemically substituted M-type hexaferrite $SrFe_{12-x}Cr_xO_{19}$, coexistence of long-range ordered ferrimagnetic phase and spin-glass phase was proposed on the basis of a Mössbauer studies at 300 K and 4.2 K [17]. More recently, spin-glass transition in $BaFe_{12-}$

$_xSc_xO_{19}$ has been reported around 50 K [141]. In a non-iron containing system $SrCr_{9p}Ga_{12-9p}O_{19}$, isostructural with M-type hexaferrites, spin-glass [18,19,21–26] and spin liquid [18,24,27] transitions have been reported at low temperatures for different values of p but this system does not show any LRO magnetic phase. In $BaCo_6Ti_6O_{19}$ also a spin-glass phase has been reported [20].

Quantum Phase Transitions

Ideally, a quantum phase transition occurs at 0 K but even above absolute zero, the quantum fluctuations coexist with the thermal fluctuations in the quantum critical regime. In this regime, one observes exotic quantum phenomena bearing signature of quantum fluctuations [142–149]. The M-type hexaferrites have also been reported to exhibit several quantum phenomena at low temperatures [7,14–16,150]. Shen et al. [14] investigated the temperature dependence of the real part of the dielectric permittivity (ε′) of flux-grown $BaFe_{12}O_{19}$ single-crystals [7,14]. The behaviour of ε_c'(T) along the c-axis of $BaFe_{12}O_{19}$ with decreasing temperature is shown in Fig. 1.20(b) [14]. Evidently ε_c' of

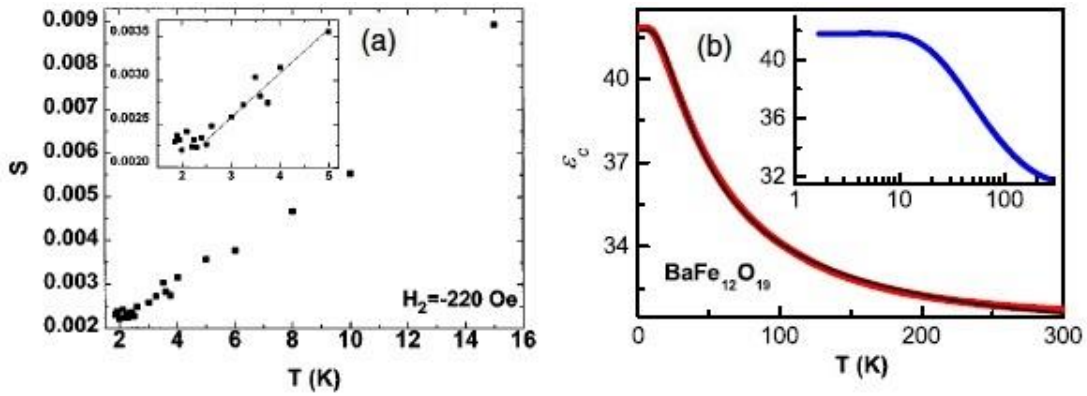

Figure 1.20: (a) Variation of the magnetic viscosity *S* with temperature. Inset shows the behaviour of *S* on the zoomed scale [28]. (b) The c-axis dielectric permittivity ε_c as a function of temperature for $BaFe_{12}O_{19}$. Inset of (b) shows the same plot with a logarithmic scale in temperature [14].

$BaFe_{12}O_{19}$ increases with decreasing temperature but becomes temperature-independent below ~10 K. This was taken to indicate quantum paraelectric behaviour in analogy with the quantum paraelectric $SrTiO_3$ [49]. The dielectric constant in the ab-plane ($\varepsilon'_{ab}(T)$), on the contrary, decreases with decreasing temperature. Subsequently, Rowley et al. [150] reported a very diffuse anomaly based on an upturns in $1/\varepsilon'_c$ below 6 K in single crystal of $BaFe_{12}O_{19}$. Cao et al. [15], on the other hand, reported a relatively sharper anomaly in $\varepsilon'_c(T)$ around 1.4 K. Shen et al. [7] measured thermal conductivity (κ) along the ab-plane of the single crystals of $BaFe_{12}O_{19}$ in the temperature range 66 mK to 1.0 K. Based on the analysis of the thermal conductivity (κ) data, they suggested that κ contains contributions not only from phonons but also an extra contribution due to non-phonon type low energy excitations below 0.6 K. The extracted excess thermal conductivity κ^* was found to be magnetic field-independent with an exponential temperature dependence (shown in Fig. 1.21) as per the following equation:

$$\kappa^* = \kappa - \beta T^3 = \alpha \exp\left(\frac{-\Delta}{k_b T}\right), \qquad \text{.....(1.5)}$$

where α and β are constants while Δ represents the excitation energy gap. Such an exponential behaviour of κ^* has been observed in the geometrically frustrated magnets where quantum spin liquid (QSL) phase has been reported [151]. In analogy with QSL, it was argued by Shen et al. [7] that the excess thermal conductivity arises due to quantum electric dipole liquid (QEDL) phase of $BaFe_{12}O_{19}$. Interestingly, in a hypothetical compound with magnetoplumbite structure, $SrCr_{12}O_{19}$ which gets stabilised through Ga substitution, a spin liquid phase at low temperatures has been confirmed by muon spin relaxation and specific heat studies due to the presence of frustrated kagome bilayer configuration in its magnetic structure [21,27]. However, it has not been possible to synthesize this compound without Ga substitution above a critical

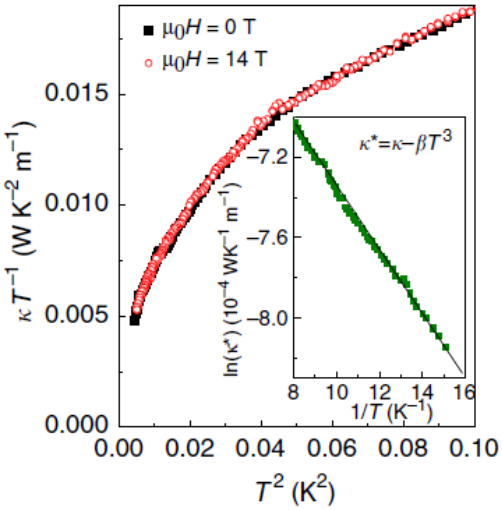

Figure 1.21: The kT^{-1} versus T^2 plot in the lowest temperature region in the presence of 0 T and 14 T applied along c-axis. The inset shows the Arrhenius plot of $k^* = k - \beta T^3$ below ~125 mK [7].

composition [18,19,21,22,24,25,152]. Zhang et al. [28] measured the low-temperature magnetic relaxations on flux-grown single crystals of $BaFe_{12}O_{19}$ and $Ba(Fe_{10.2}Sn_{0.74}Co_{0.66})O_{19}$ and extracted the temperature dependence of magnetic viscosity as shown in Fig. 1.20(a). The inset of this figure reveals that the magnetic viscosity may have become temperature independent below 2.5 K which led these workers to propose quantum tunneling of magnetic domain walls at low temperature [28]. Further, Ga^{3+} substitution at the Fe^{3+} site in $PbFe_{12}O_{19}$ has been reported to lower the ferrimagnetic phase transition temperature as per a power-law [8]:

$$T_C \approx (1 - \frac{x}{x_c})^{2/3}, \qquad \text{.....(1.6)}$$

where critical composition $x_c \sim 8.6$ of Ga at which T_c becomes zero has been identified as a magnetic quantum critical point [8].

Using numerical simulations, Shen et al. [14] argued that Fe^{3+} should occupy off-centre positions in the FeO_5 bipyramid at low temperatures and it should not fluctuate

between the two 4e Wyckoff sites as proposed in earlier studies [119,121,122,124–126,153]. This off-centred Fe^{3+} may induce a local electric dipole in the unit cell which may undergo an ordering at low temperatures. The ground state density functional theory calculations [16] suggest that electric dipoles may get aligned along the c-axis with ferroelectric correlations with their ab-plane component having antiferroelectric correlations. Finite temperature Monte Carlo simulations reveal the possibility of a LRO transition around 3 K. Further, the simulations by the same workers reveal that the ferroelectric state of $BaFe_{12}O_{19}$ may be stabilised even at room temperature by suitable chemical substitutions or strain engineering. These theoretical predictions are apparently in contradiction to the existing experimental report, as the quantum Barret's law fit to the temperature dependence of ε'_c(T) reveals that T_0, which is equivalent to Curie-Weiss temperature for the classical Curie-Weiss law, has got negative sign suggesting antiferroelectric correlations along the c-axis [7,14].

Multifunctional Behaviour

The M-type hexaferrites have been reported to be essentially collinear ferrimagnetic materials with very high Curie transition temperature with T_c lying [12,131]. Both the M-H and P-E hysteresis loops have been reported in $BaFe_{12}O_{19}$, $SrFe_{12}O_{19}$, $PbFe_{12}O_{19}$ and (La, Ba)$Fe_{12}O_{19}$ hexaferrites at room temperature suggesting their multiferroicity [154–159]. Using temperature dependent Raman scattering studies on $BaFe_{12}O_{19}$ and $Ba(Fe_{10.5}In_{1.5})O_{19}$ hexaferrites at high temperatures, spin-phonon coupling at the ferrimagnetic transition temperature [160,161] as well as around 80 K [137] has been reported. In another study, Sc doping in $BaFe_{12}O_{19}$ has been shown to reduce the ferrimagnetic transition temperature [29,33,141] and induce collinear to longitudinal type conical structure on lowering the temperature [29]. In such compositions, emergence of electrical polarization through the inverse Dzyaloshinskii-

Moriya mechanism has been reported in the presence of transverse external magnetic field which transforms the longitudinal conical structure into a transverse conical structure [29,33,141]. Ga substituted $PbFe_{12}O_{19}$ has been reported to exhibit relaxor ferroelectric behaviour and exchange striction [31]. Multiferroic behaviour in doped and undoped M-type hexaferrites has also been reported through direct measurements such as change in magnetization with applied electric field [30,33,116,162], current-induced non-linear magnetoelectric effect [163], change in capacitance/dielectric constant with applied magnetic fields [141] and appearance of magnetoelectric voltage on application of magnetic field [164].

1.12 Objectives of the Present Work

It is evident from the foregoing that the low temperature behaviour of the undoped M-type hexaferrite $BaFe_{12}O_{19}$ has not been investigated systematically, except for the isolated reports based on Raman, Mössbauer and dc magnetization measurements. Anomalies in the dc M(T) has been claimed around 50 K, 80 K [137] and 150 K [140] while anomalous behaviour in the intensity of the magnon modes has been reported around 80 K and 200 K [138]. The sole $\chi(\omega, T)$ study on nano- and micro-crystalline $BaFe_{12}O_{19}$ polycrystals revealed peaks around 125 K and 50 K but without any shift of the peak temperature with frequency. Further, the magnetic structure of $BaFe_{12}O_{19}$ has all along been assumed [e.g. see 29] to be collinear as per Gorter model [39]. No attempt has been made to search for spin canting and study the consequences of spin canting in unsubstituted $BaFe_{12}O_{19}$. The present investigation was undertaken to critically examine the collinear magnetic structure of $BaFe_{12}O_{19}$ and investigate its consequences on the low temperature behaviour of this compound in the temperature range 1.5 K to 300 K. For this we have carried out X-ray absorption spectroscopy (XAS) and X-ray magnetic circular dichroism (XMCD), X-ray and neutron powder diffraction, single-crystal neutron

scattering, dc and ac magnetic susceptibility, dielectric and specific heat studies using in-house facilities as well as advanced facilities at Petra-III, DESY, Hamburg, FRM-II, Garching and ISIS at Rutherford Appleton Laboratory, Harwell. Polycrystalline powder, sintered ceramic and single crystals of $BaFe_{12}O_{19}$ were used in these measurements. These investigations have not only confirmed the non-collinear magnetic structure of $BaFe_{12}O_{19}$ with incommensurate longitudinal conical magnetic structure but have also led to the discovery of five spin-glass transitions and quantum electric dipole glass state, besides confirming the QEDL state using specific heat studies and occurrence of two magnetic transitions around 50 K and 200 K predicted by the earlier workers. The results of the present investigation are presented in the following eight chapters of this thesis.